Published in final edited form as:
Int J Radiat Oncol Biol Phys. 2013 November 1; 87(3): 562–569. doi:10.1016/j.ijrobp.2013.06.2042.

A Comparison of Amplitude-based and Phase-based Positron Emission Tomography Gating Algorithms for Segmentation of Internal Target Volumes of Tumors Subject to Respiratory Motion

Shyam S. Jani, MS[*], **Clifford G. Robinson, MD**[†], **Magnus Dahlbom, PhD**[‡], **Benjamin M. White, PhD**[*], **David H. Thomas, PhD**[*], **Sergio Gaudio, PhD**[*], **Daniel A. Low, PhD**[*], and **James M. Lamb, PhD**[*]

[*]Department of Radiation Oncology, David Geffen School of Medicine, University of California, Los Angeles, California

[†]Department of Radiation Oncology, Siteman Cancer Center, Washington University in St Louis, St Louis, Missouri

[‡]Department of Molecular and Medical Pharmacology, David Geffen School of Medicine, University of California, Los Angeles, California

Abstract

Purpose—To compare quantitatively the accuracy of tumor volume segmentation in amplitude-based and phase-based respiratory gating algorithms in respiratory-correlated positron emission tomography (PET).

Methods and Materials—List-mode fluorodeoxyglucose-PET data was acquired for 10 patients with a total of 12 fluorodeoxyglucose-avid tumors and 9 lymph nodes. Additionally, a phantom experiment was performed in which 4 acrylic spheres with inner diameters ranging from 1 to 4 cm were imaged as they underwent 1-dimensional motion based on 2 measured patient breathing trajectories. PET list-mode data were gated into 8 bins using 2 amplitude-based (equal amplitude bins [A1] and equal counts per bin [A2]) and 2 temporal phase-based gating algorithms. Gated images were segmented using a commercially available gradient-based technique and a fixed 40% threshold of maximum uptake. Internal target volumes (ITVs) were generated by taking the union of all 8 contours per gated image. Segmented phantom ITVs were compared with their respective ground-truth ITVs, defined as the volume subtended by the tumor model positions covering 99% of breathing amplitude. Superior-inferior distances between sphere centroids in the end-inhale and end-exhale phases were also calculated.

Results—Tumor ITVs from amplitude-based methods were significantly larger than those from temporal-based techniques (P= .002). For lymph nodes, A2 resulted in ITVs that were significantly larger than either of the temporal-based techniques (P<*.0323*). A1 produced the largest and most accurate ITVs for spheres with diameters of ≥2 cm (P = .002). No significant difference was shown between algorithms in the 1-cm sphere data set. For phantom spheres, amplitude-based methods recovered an average of 9.5% more motion displacement than temporal-

---

Reprint requests to: Shyam S. Jani, MS, 200 UCLA Medical Plaza, Suite B265, Box 956951, Los Angeles, CA 90095. Tel: (858) 342-7476.

Conflict of interest: none.

based methods under regular breathing conditions and an average of 45.7% more in the presence of baseline drift (*P<.001*).

Conclusions—Target volumes in images generated from amplitude-based gating are larger and more accurate, at levels that are potentially clinically significant, compared with those from temporal phase-based gating.

Introduction

As early as 1999, positron emission tomography (PET) was shown to have a high impact on the delineation of radiation therapy target volumes for lung cancer, primarily by altering the inclusion of mediastinal and hilar lymph nodes and also for solid tumors having CT-ambiguous morphology, such as those with tumor-associated atelectasis (1–4). Adaptive PET imaginge—based dose-escalation techniques have been proposed in which tumor subregions, identified by elevated metabolism or other functional signatures, are targeted with increased dose (5, 6). Respiratory-gated PET is known to improve the measurement of lesion uptake and tumor volume, making PET imaging more accurate for those applications (7–10). More recent clinical studies have used four-dimensional (4D) PET (multiple gated images correlated to respiratory motion) to derive internal target volumes for tumors subject to respiratory motion (11, 12). 4D-PET requires the gating of coincidence data in a single PET scan, acquired in list-mode format according to a surrogate of breathing, into multiple images. Gating methods based on temporal phase and on breathing surrogate amplitude have both been demonstrated in PET (13–16). Temporal-based gating methods have previously been shown to be inferior to amplitude-based techniques using a metric of observed displacement of the heart muscle due to respiration (16). An amplitude-based quiescent-phase gating (14) has been reported to be superior to temporal phase-based gating in recovering tracer uptake; however, this method produces a gated image only in the quiescent, or resting end-exhalation, phase of breathing. Another resting-phase method was reported to have $\mathrm{SUV}_{\mathrm{max}}$ comparable to temporal phase gated 4D-PET (13). To the best of our knowledge, no study has been performed to compare the accuracy of amplitude-based and phase-based PET gating for the purpose of generating internal target volumes of tumors subject to respiratory motion. This report uses phantom and patient data to compare 4 gating techniquesd—2 amplitude based and 2 phase basedd—in the context of mobile lung tumors. Our results can be used to guide selection of an appropriate gating algorithm to optimize the accuracy of 4D-PET imaging in a clinical setting.

Methods and Materials

A hybrid PET/compute tomography (CT) scanner (Biograph TruePoint/TrueView 64; Siemens Medical Solutions) was used for the experimental protocols, which included both patient and phantom scans. The PET system used was a multiring LSO scanner that operated in a 3-dimensional acquisition mode, characterized by a 21.6-cm longitudinal field of view and a 67-cm transverse field of view. The CT system was a 40-slice scanner with 40 detector rows and a rotation time of 0.37 seconds. The patient scanning protocol included a helical CT scan, an axial 4D CT, and a PET list-mode acquisition.

Setup and data acquisition

The phantom consisted of 4 CAB plastic spheres (Phantom Laboratory, Salem, NY), with inner diameters of 1, 2, 3, and 4 cm, affixed inside a 9.3-L acrylic cylinder. The spheres and cylinder were filled with solutions of^{11} C and^{18} fluorodeoxyglucose (FDG), respectively, to generate a time-varying signal-to-background ratio. The system was attached to a custom-built robotic arm that underwent 1-dimensional motion in the superior-inferior direction. Input motion was based on patient breathing trajectories acquired via a pneumatic bellows device (Philips Medical Systems; Fig. 1). The bellows is a small hollow rubber tube strapped around the patient's abdomen. As it expands and contracts from breathing motion, the resultant pressure change is read by a transducer that provides a voltage signal proportional to the bellows' expansion.

The bellows signal was recorded synchronously with PET data acquisition using an external data-acquisition (DAQ) system operating at a sampling frequency of 100 Hz (Labview; National Instruments Corporation, Austin, TX). The respiratory trigger input of the PET scanner accepts transistor-transistor logic (TTL) voltage levels and inserts trigger words in the list-mode file when a high TTL level is received. Synchronization between the PET scanner and the external DAQ system was achieved by using the DAQ system's analog output to generate TTL level pulses at random time intervals in the range of 1 to 5 seconds. The pulses were then sent to the PET scanner and the DAQ system's digital input. The PET list-mode file was synchronized with the breathing DAQ file by computing the offset between their 2 nominal timestamps such that the times of the randomly distributed triggers matched.

Ten patients with a total of 12 FDG-avid lung tumors and 9 mediastinal and hilar lymph nodes were also imaged as part of an institutional review board—approved study at XXXX. Patients with relatively small lower-lobe tumors were selected for enrollment because the purpose of the study was to image highly mobile tumors. All patients fasted at least 4 hours before scanning. PET list-mode data was acquired 60 min after administration of approximately 10 μCi of FDG activity. A single 21.6-cm bed position was imaged for 12 minutes for the 4D-PET scans to obtain sufficient coincidence event statistics after gating, while simultaneously avoiding longer scans than what patients could easily tolerate, which might increase the probability of patient movement during scans. Breathing surrogate traces were examined for discontinuities that would arise from patient movement; no such discontinuities were observed.

Image reconstruction

List-mode data were gated according to the abdominal bellows signal. Four gating methods (2 phase-based and 2 amplitude-based, described subsequently) were compared. Each method used 8 gating windows with 2 minutes of list-mode data for the phantom and 12 minutes for the patients. The gating was performed with custom software written in MATLAB (Mathworks; R2010b). Gated list-mode files were reconstructed into emission images using Siemens reconstruction software with the same algorithms used for clinical image reconstruction (AW-OSEM, 4 subsets, 8 iterations). Pixel size was 4.07 × 4.07 × 2.03 mm^3. Images were reconstructed without attenuation correction to avoid bias resulting from incorrect phase-matching to amplitude or phase-gated 4D-CT Images were smoothed with a 5-mm Gaussian filter.

Gating method A1: amplitude-based gating, equal-amplitude windows

The amplitude range of the patient's breathing surrogate signal during the PET acquisition was divided evenly into 8 bins (Fig. 2a). This method limited the intrawindow motion to a uniform level, which was advantageous for measuring tumor motion and volume. However, some of the gating windows contained small numbers of coincidence events (typically at end-inhalation), leading to excess image noise in those windows. To minimize the effect of atypical high-amplitude breaths, only windows within the breathing amplitude range from minimum amplitude to 99th percentile were used for image reconstruction.

Gating method A2: amplitude-based gating, equal events per window

In this gating method, 8 amplitude windows were chosen such that each window contained an equal number of coincidence events. This resulted in closely spaced gating windows in the quiescent phase of breathing and greater amplitude spacing per window near inhalation (Fig. 2b). Although this was expected to provide an approximately uniform noise performance per image, there would also be an uneven amount of intrawindow motion.

Gating methods T1 and T2: temporal phase-based gating

For temporal phase-based gating, breathing peaks in the surrogate signal were first identified using an automated method (17). The signal trace was examined visually, and any missing or extraneous peaks were added and deleted, respectively. The breathing cycle was divided into 8 gating windows with divisions between windows evenly spaced between breathing peaks. By definition, this conventional gating method, denoted here as T1, split the data from breathing peaks into 2 gating windows (Fig. 2c). We also examined a second temporal-based method, called T2, where the divisions between gating windows were placed at the midpoint between the gating window divisions of method T1, thus including data surrounding a breathing peak into a single gating window (Fig. 2d). Both T1 and T2 resulted in uniform number of events, but varying intrawindow motion, per gated image.

Image segmentation and analysis

Image segmentation and analysis was performed using a commercial software package (MIM v5.6.4, MIM Software, Cleveland, OH). Gated phantom images were segmented using MIM's PET Edge tool, a semiautomatic gradient-based technique that defines tumor edges using spatial derivatives (18), and a fixed 40% threshold technique (19, 20). Patient images were segmented using only PET Edge because the fixed threshold technique failed for lymph nodes, segmenting the entire mediastinum in several cases. Motion displacement between end-inhale and end-exhale bins was calculated by measuring the distance between sphere centroids (superior-inferior distance for phantom data, 3-dimensional distance for patient data). Internal target volumes (ITVs) were generated by joining the 8 contours from the individual 8 gated images via union operators. Tumor model ITVs in the phantom data were compared with their calculated ground-truth ITVs based on the known sphere volume and motion trajectory. To avoid the effects of outlier breaths, the top and bottom 0.5th percentile of breathing amplitude was removed when defining the ground-truth ITV, resulting in 99% of breathing amplitude coverage. For the phantom experiment, images with varying signal-to-background ratios (SBRs) ranging from high to low (25:1, 13:1, and 5:1) were examined.

Statistical analysis

To compare differences in segmented ITVs between algorithms for the patient and phantom datasets, 2-way analysis of variance and Tukey's range tests and their corresponding nonparametric tests of Kruskal-Wallis and Mann-Whitney-Wilcoxon were used. Analysis of variance was used to compare algorithm differences in recovering target motion amplitude for the phantom data set. Because of target size variability in the patient data set, the ITV of each tumor and lymph node was standardized for the purposes of the statistical analysis by dividing the ITV generated by each algorithm by the T1 ITV.

Results

Table 1 shows the average percentage of recovered superior-inferior motion displacement of end-exhale and end-inhale images (columns 1–2) for the phantom data. Amplitude-based methods recovered motion ranges higher than temporal phase-based methods by an average of 9.5% (P<.001) and 45.7% (P<.001) for trajectories 1 and 2, respectively. A1 demonstrated the greatest robustness in the presence of irregular breathing with baseline drift by recovering 94% of target motion displacement (P<.001).

The average ratio of measured to ground-truth ITVs using PET Edge (columns 3–5) and 40% threshold (columns 6–8) are also shown in Table 1. Values are averaged across both trajectory types and the 3 SBRs. Selected SBR values did not have a significant effect on algorithm performance (P=.160). Across both segmentation techniques, A1 demonstrated the largest ITV segmentation for sphere groups 1 to 4 cm and 2 to 4 cm (P= .019, P=.002). No significant difference was observed between algorithms for the 1-cm group. Figure 3 shows an example of gated end-inhale images of phantom spheres undergoing irregular breathing motion for all the gating methods.

Across all tumors and lymph nodes, amplitude-based methods produced ITVs that were significantly larger than temporal-based methods (P<.001; Table 2). The tumor data set yielded the same results (P<.001). For the lymph nodes, A2 was significantly larger than T1 (P=.002) and T2 (P=.0323), and A1 was significantly larger than T1 (P=.009). Figure 4 shows gated images of a selection of tumors and lymph nodes.

Discussion

In the patient data set, amplitude-based gating produced significantly larger ITVs than phase-based gating. Although no ground-truth target volume was available for the patient images, we observed a consistent undersegmentation in the phantom data for sphere diameters of ≥2 cm for both the gradient-based and fixed 40% threshold methods, suggesting that larger ITVs are likely more accurate in the patient data set. Furthermore, even lacking other information, given a choice between a possible under- or oversegmentation, it would likely be preferable to err toward oversegmentation to prevent a marginal miss of the target and thereby increase the probability of local tumor control.

For phantom spheres ≥2 cm in diameter, A1 was found to produce the largest and most accurate ITVs. Because the fixed amplitude-range windows in A1 resulted in uneven coincidence event statistics per gate, it also led to increased noise in images such as end-inhalation. Methods T1 and T2 resulted in a uniform noise level in all gating windows, but captured a smaller degree of target motion. Method A2 also produced gated images with uniform noise but captured more motion than temporal-based methods, especially under conditions of irregular breathing (Table 1). The ideal balance between image quality and recovery of motion displacement is a clinical trade-off that depends in part on the preference of individual physicians and as such cannot be answered by this study. Dawood et al (16) showed that amplitude-based respiratory gating resulted in a larger measured heart motion in cardiac PET. The present study not only confirms these results for lung tumors and lymph nodes in both patient and phantom data, but goes beyond that work to quantify the benefit of amplitude-based gating with respect to segmentation of target volumes.

We observed that volume segmentations of the small sphere and the larger (>1 cm) spheres were qualitatively and quantitatively different, and so they were analyzed separately. The 1 cm sphere tended to be oversegmented by both segmentation techniques, and the degree of oversegmentation was highly variable; this was likely due to the partial volume effect for small targets in PET imaging (21). A statistical analysis showed that none of the gating algorithms for the 1-cm sphere was significantly better than the others, although A2 had the least variability and smallest amount of oversegmentation. In the patient data set, both amplitude-based methods produced ITVs that were significantly larger than those from both temporal phase-based methods for the solid tumors. Similar results were observed for the lymph nodes, with the exception being that A1 was not significantly different from T2 (P=.12). Because the average motion and size of the nodes were smaller than that of the tumors, all individual algorithm differences may be more difficult to detect. However, average lymph node ITVs were greater than those of the 1-cm sphere and were less likely to be susceptible to the partial volume effect in volume segmentation. Together, the lymph node and 1-cm sphere results suggest that A2 could better represent volumes of small mobile targets, but additional studies are needed to confirm these results.

Gradient-based PET image segmentation algorithms are generally regarded as more accurate than fixed percentage threshold based segmentation (18, 22, 23). Because it is still used in clinical practice, we included a fixed 40% threshold segmentation algorithm to show that the comparison of amplitude and phase gating was robust to changes in the details of volume segmentation. Determination of the optimal PET segmentation algorithm has been thoroughly studied (24) but is yet undetermined and therefore beyond the scope of this investigation.

One limitation of this study is that the effect of the number of gating windows was not examined. Increasing the number of gating windows beyond 8 would be expected to increase the motion recovery of both amplitude-based and phase-based gating at the expense of increased image noise. We chose 8 gating windows because this was found to be effective in capturing motion displacement in a cardiac PET study (15) and obtaining motion-free images in a respiratory gated 4D-PET/CT study (25). In addition, only nonattenuation corrected images were examined in this study, although segmentation can also be performed on PET images with attenuation correction applied. If attenuation correction is performed on gated PET using CT images, the CT images should be phase-matched to the PET images. The quality of the 4D-CT images and the phase-matching could influence the segmentation of target volumes differentially between amplitude-gated and phase-gated PET images. A number of studies have shown that amplitude-based 4D-CT sorting is more accurate than phase-based 4D-CT sorting (26–29), so it would be expected that use of attenuation corrected images would not alter the conclusions of the present study; however, additional studies should be performed to confirm these findings for phase-matched 4D-PET/CT.

Conclusions

Compared with phase-based gating, amplitude-based gating produced PET images that led to larger ITVs for lung tumors. For lymph nodes and mobile phantom spheres ≥2 cm in diameter, amplitude-based methods resulted in larger and more accurate ITVs but not at statistically significant levels for both amplitude-based algorithms in all cases. Amplitude-based gating resulted in ITVs approximately 10% and nearly 20% larger than phase-based gating for the lymph nodes and the tumors, respectively. For moving 1-cm spheres, there was no clear difference in ITV generation from the different algorithms. Amplitude-based gating algorithms that use equal amplitude range windows produce the largest ITVs but also result in images with more noise in the end-inhalation breathing phase.

Acknowledgments

We thank Judson Jones, PhD, Siemens Molecular Imaging, for providing stand-alone PET reconstruction modules.

This work was supported in part by National Institutes of Health Grants R01CA096679 and R01CA116712.

References

1. Nestle U, Walter K, Schmidt S, et al. 18F-deoxyglucose positron emission tomography (FDG-PET) for the planning of radiotherapy in lung cancer: high impact in patients with atelectasis. Int J Radiat Oncol Biol Phys. 1999; 44:593–597. [PubMed: 10348289]
2. Vanuytsel LJ, Vansteenkiste JF, Stroobants SG, et al. The impact of (18) F-fluoro-2-deoxy-D-glucose positron emission tomography (FDG-PET) lymph node staging on the radiation treatment volumes in patients with non-small cell lung cancer. Radiother Oncol. 2000; 55:317–324. [PubMed: 10869746]
3. Mah K, Caldwell CB, Ung YC, et al. The impact of (18)FDG-PET on target and critical organs in CT-based treatment planning of patients with poorly defined non-small-cell lung carcinoma: A prospective study. Int J Radiat Oncol Biol Phys. 2002; 52:339–350. [PubMed: 11872279]
4. Bradley J, Thorstad WL, Mutic S, et al. Impact of FDG-PET on radiation therapy volume delineation in non-small-cell lung cancer. Int J Radiat Oncol Biol Phys. 2004; 59:78–86. [PubMed: 15093902]
5. Feng M, Kong F-M, Gross M, et al. Using fluorodeoxyglucose positron emission tomography to assess tumor volume during radiotherapy for non—small-cell lung cancer and its potential impact on adaptive dose escalation and normal tissue sparing. Int J Radiat Oncol Biol Phys. 2008; 73:1228–1234. [PubMed: 19251094]
6. Holloway CL, Robinson D, Murray B, et al. Results of a phase I study to dose escalate using intensity modulated radiotherapy guided by combined PET/CT imaging with induction chemotherapy for patients with non-small cell lung cancer. Radiother Oncol. 2004; 73:285–287. [PubMed: 15588872]
7. Nehmeh SA, Erdi YE, Ling CC, et al. Effect of respiratory gating on quantifying PET images of lung cancer. J Nucl Med. 2002; 43:876–881. [PubMed: 12097456]
8. Boucher L, Rodrigue S, Lecomte R, et al. Respiratory gating for 3-dimensional PET of the thorax: Feasibility and initial results. J Nucl Med. 2004; 45:214–219. [PubMed: 14960638]
9. Nehmeh SA, Erdi YE, Pevsner A, et al. Four-dimensional (4D) PET/CT imaging of the thorax. Med Phys. 2004; 31:3179–3186. [PubMed: 15651600]
10. Wolthaus JWH, van Herk M, Muller SH, et al. Fusion of respiration-correlated PET and CT scans: Correlated lung tumour motion in anatomical and functional scans. Phys Med Biol. 2005; 50:1569–1583. [PubMed: 15798344]
11. Lamb JM, Robinson C, Bradley J, et al. Generating lung tumor internal target volumes from 4D-PET maximum intensity projections. Med Phys. 2011; 38:5732–5737. [PubMed: 21992387]
12. Aristophanous M, Yap JT, Killoran JH, et al. Four-dimensional positron emission tomography: Implications for dose painting of high-uptake regions. Int J Radiat Oncol Biol Phys. 2011; 80:900–908. [PubMed: 20950956]
13. van Elmpt W, Hamill J, Jones J, et al. Optimal gating compared to 3D and 4D PET reconstruction for characterization of lung tumours. Eur J Nucl Med Mol Imaging. 2011:1–13. [PubMed: 21104245]
14. Liu C, Alessio A, Pierce L, et al. Quiescent period respiratory gating for PET/CT. Med Phys. 2010; 37:5037–5043. [PubMed: 20964223]
15. Dawood M, Buther F, Stegger L, et al. Optimal number of respiratory gates in positron emission tomography: a cardiac patient study. Med Phys. 2009; 36:1775–1784. [PubMed: 19544796]
16. Dawood M, Büther F, Lang N, et al. Respiratory gating in positron emission tomography: a quantitative comparison of different gating schemes. Med Phys. 2007; 34:3067. [PubMed: 17822014]
17. Lu W, Nystrom MM, Parikh PJ, et al. A semi-automatic method for peak and valley detection in free-breathing respiratory waveforms. Med Phys. 2006; 33:3634–3636. [PubMed: 17089828]
18. Werner-Wasik M, Nelson AD, Choi W, et al. What is the best way to contour lung tumors on PET scans? Multiobserver validation of a gradient-based method using a NSCLC digital PET phantom. Int J Radiat Oncol Biol Phys. 2012; 82:1164–1171. [PubMed: 21531085]

19. Erdi YE, Rosenzweig K, Erdi AK, et al. Radiotherapy treatment planning for patients with non-small cell lung cancer using positron emission tomography (PET). Radiother Oncol. 2002; 62:51–60. [PubMed: 11830312]
20. Erdi YE, Mawlawi O, Larson SM, et al. Segmentation of lung lesion volume by adaptive positron emission tomography image thresholding. Cancer. 1997; 80(suppl 12):2505–2509. [PubMed: 9406703]
21. Teo BK, Seo Y, Bacharach SL, et al. Partial-volume correction in PET: Validation of an iterative postreconstruction method with phantom and patient data. J Nucl Med. 2007; 48:802–810. [PubMed: 17475970]
22. Wanet M, Lee JA, Weynand B, et al. Gradient-based delineation of the primary GTV on FDG-PET in non-small cell lung cancer: A comparison with threshold-based approaches, CT and surgical specimens. Radiother Oncol. 2011; 98:117–125. [PubMed: 21074882]
23. Geets X, Lee JA, Bol A, et al. A gradient-based method for segmenting FDG-PET images: Methodology and validation. Eur J Nucl Med Mol Imaging. 2007; 34:1427–1438. [PubMed: 17431616]
24. Zaidi H, El Naqa I. PET-guided delineation of radiation therapy treatment volumes: A survey of image segmentation techniques. Eur J Nucl Med Mol Imaging. 2010; 37:2165–2187. [PubMed: 20336455]
25. Bettinardi V, Rapisarda E, Gilardi MC. Number of partitions (gates) needed to obtain motion-free images in a respiratory gated 4D-PET/CT study as a function of the lesion size and motion displacement. Med Phys. 2009; 36:5547–5558. [PubMed: 20095267]
26. Wink N, Panknin C, Solberg TD. Phase versus amplitude sorting of 4D-CT data. J Appl Clin Med Phys. 2006; 7:77–85. [PubMed: 16518319]
27. Lu W, Parikh PJ, Hubenschmidt JP, et al. A comparison between amplitude sorting and phase-angle sorting using external respiratory measurement for 4D CT. Med Phys. 2006; 33:2964–2974. [PubMed: 16964875]
28. Abdelnour AF, Nehmeh SA, Pan T, et al. Phase and amplitude binning for 4D-CT imaging. Phys Med Biol. 2007; 52:3515–3529. [PubMed: 17664557]
29. Li H, Noel C, Garcia-Ramirez J, et al. Clinical evaluations of an amplitude-based binning algorithm for 4DCT reconstruction in radiation therapy. Med Phys. 2012; 39:922–932. [PubMed: 22320802]

Summary

Respiratory-gated positron emission tomography has the potential to aid target volume delineation for tumors subject to respiratory motion. Gating is performed on either the amplitude or temporal phase of breathing. This work compares amplitude- and phase-based gating methods for internal target volume segmentation using phantom and patient images. We find that amplitude-based methods result in larger and more accurate internal target volumes and should therefore be preferred for use in radiation therapy planning.

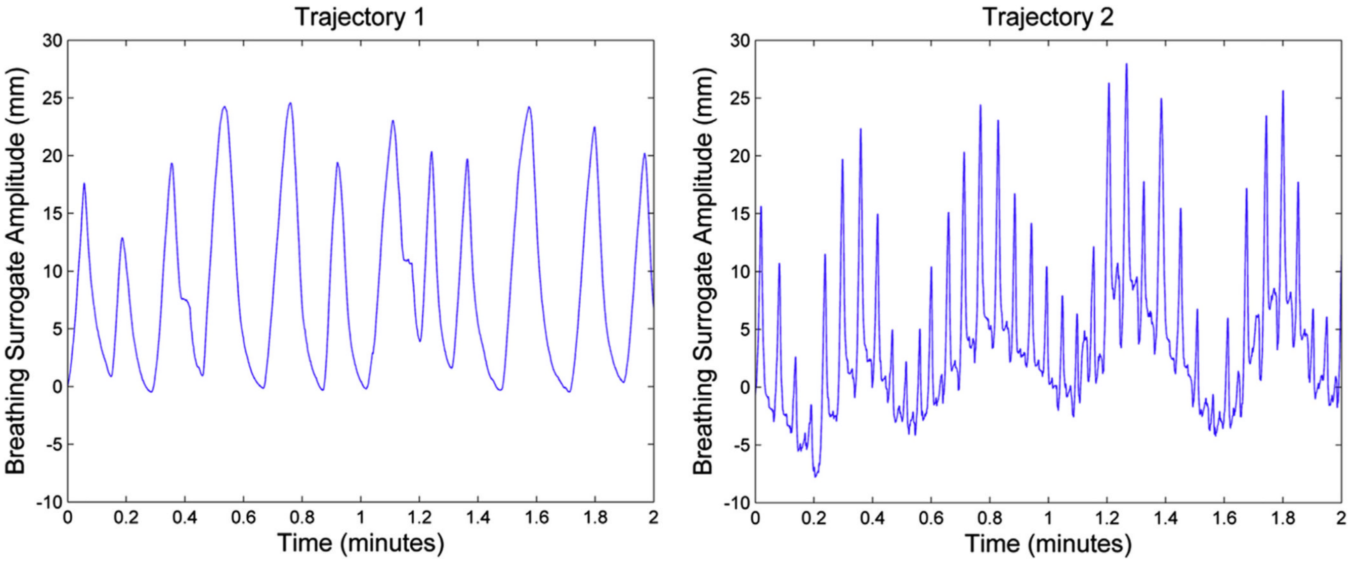

Fig. 1.

Patient-derived breathing trajectories. Trajectory 1 represents a regular breathing pattern, and trajectory 2 shows irregular breathing with baseline drift (varying end-exhale positions). Breathing motion amplitude for trajectories 1 and 2 were 25.1 and 35.8 mm, respectively. Phantom images were generated from 2 minutes of breathing motion.

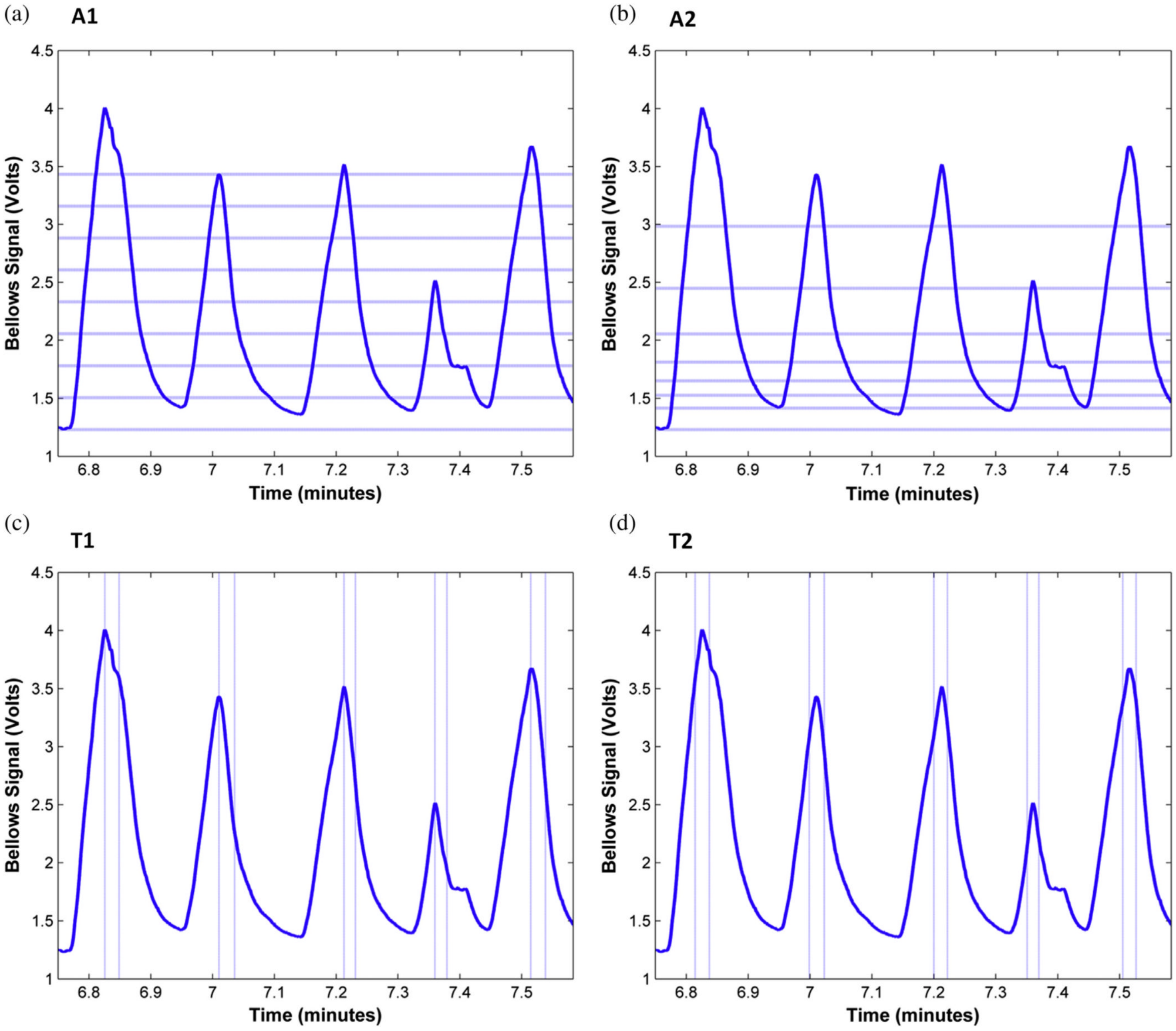

Fig. 2.

Illustration of gating algorithms on a part of patient 2’s breathing trace during positron emission tomography acquisition: algorithm A1, amplitude-based with equal amplitude windows; A2, amplitude-based with equal events per window; T1, temporal phase-based with the first gating window starting at peak inhale; T2, temporal phase-based with the first gating window centered on peak inhale. Dotted lines show the boundaries between gating windows. For clarity, only the first gating window is shown for methods T1 and T2.

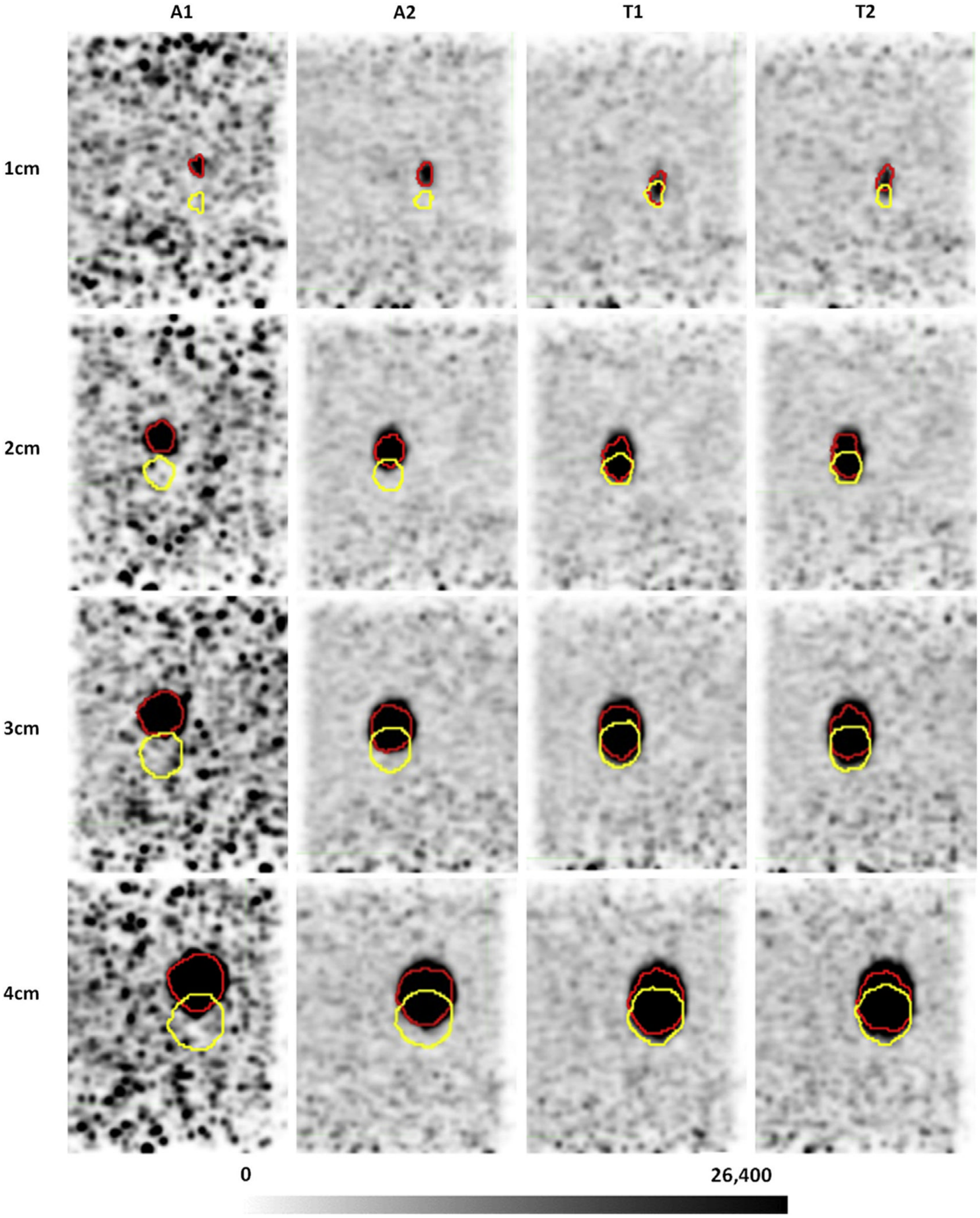

Fig. 3.

End-exhale (yellow) and end-inhale (red) contours for a high signal-to-background ratio image of phantom spheres undergoing irregular breathing motion (trajectory 2). A1 demonstrates the largest motion separation across all gating methods, although it also produces the noisiest end-inhale bin. Pixel units are Bq/mL.

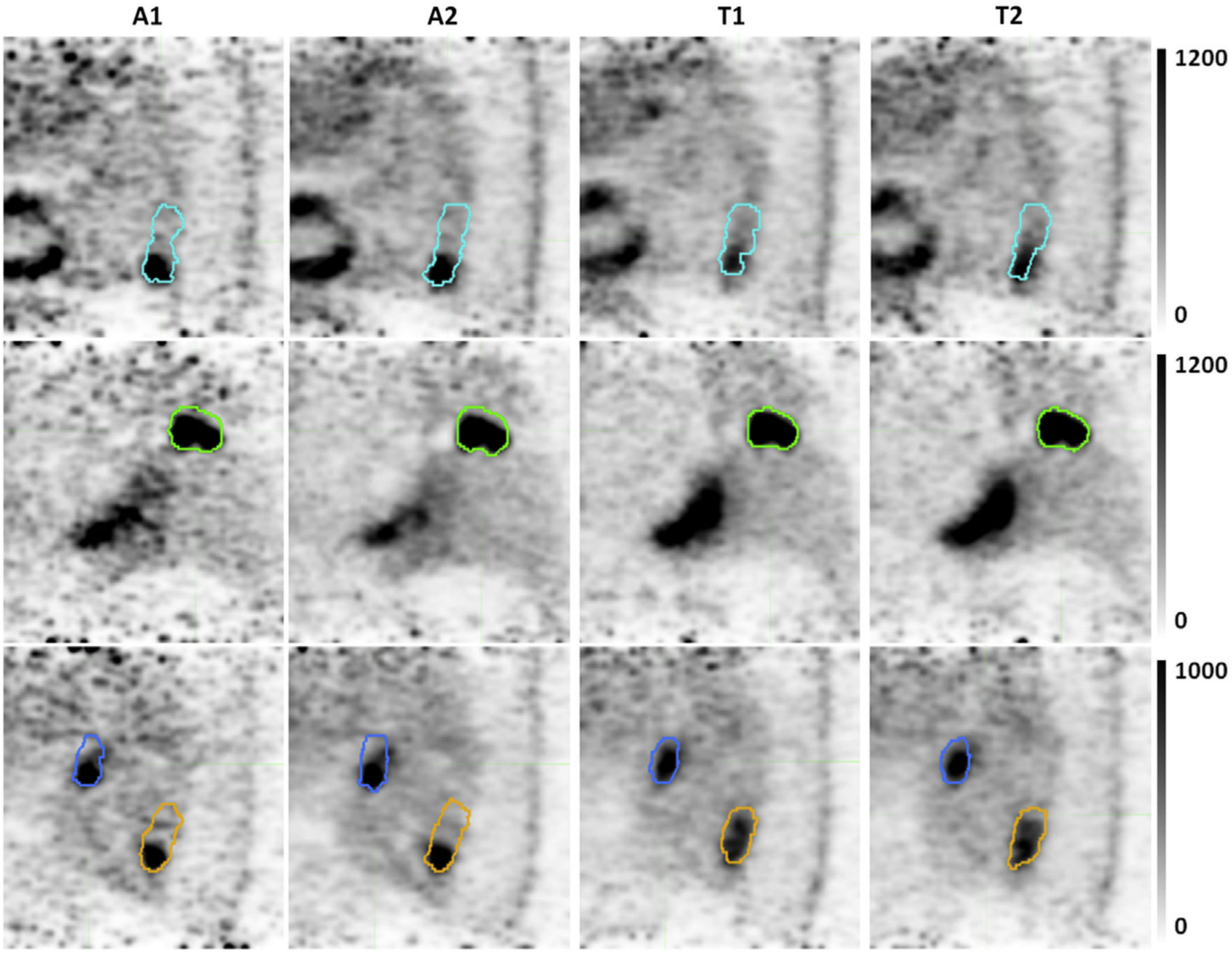

Fig. 4.

Selected slices highlighting algorithm differences in image generation and segmentation. Internal target volumes of tumor 3 (cyan), tumor 5 (green), lymph node 9 (blue), and tumor 9 (orange) registered to the end-inhale breathing phase. Pixel units are proportional to counts per second. Gated images from temporal-based algorithms have increased motion blurring artifacts.

Table 1

Measured parameters for phantom data

	Distance		ITV (PET Edge)				ITV (40% threshold)			
	Traj 1	**Traj 2**	$\mu_1 \pm \sigma_1$	$\mu_2 \pm \sigma_2$	$\mu_3 \pm \sigma_3$	$\mu_4 \pm \sigma_4$	$\mu_1 \pm \sigma_1$	$\mu_2 \pm \sigma_2$	$\mu_3 \pm \sigma_3$	$\mu_4 \pm \sigma_4$
T1	76.2%	31.3%	1.62 ± 0.51	0.83 ± 0.21	0.82 ± 0.16	0.86 ± 0.15	1.83 ± 1.05	0.70 ± 0.10	0.65 ± 0.07	0.66 ± 0.04
T2	80.2%	31.3%	1.64 ± 0.46	0.88 ± 0.18	0.83 ± 0.16	0.87 ± 0.17	2.33 ± 1.40	0.75 ± 0.22	0.67 ± 0.10	0.68 ± 0.08
A1	89.0%	94.0%	1.79 ± 0.25	1.09 ± 0.12	1.01 ± 0.07	1.03 ± 0.05	2.06 ± 1.13	0.84 ± 0.18	0.84 ± 0.10	0.83 ± 0.05
A2	86.4%	60.0%	1.39 ± 0.19	0.93 ± 0.15	0.90 ± 0.11	0.95 ± 0.10	1.68 ± 0.88	0.67 ± 0.06	0.74 ± 0.06	0.77 ± 0.03

Abbreviations: ITV = internal target volumes; PET = positron emission tomography; Traj = trajectory.

Motion displacement recovery and measured to expected ITV measurements across the 4 gating algorithms for the phantom data. PET Edge was used to segment end-exhale and end-inhale images for superior-inferior distance measurements. Images at several signal-to-background ratios were used to collect the data for sphere sizes 2 to 4 cm (trajectory 1: n = 24 per algorithm; traj 2: n = 21 for A2, n=18 for rest). ITV measurements (mean and SD) are shown for all spheres (n = 6 per sphere size per algorithm).

Table 2

Measured parameters for patient data

	Mean intensity (PROPCPS)	Max intensity (PROPCPS)	Net target motion (mm)	Target diameter (cm)	T1 ITV (cm^3)	T2 ITV (cm^3)	A1 ITV (cm^3)	A2 ITV (cm^3)
Tumor 1	441	1234	22.4	4.29	39.63	38.97	42.46	41.15
Tumor 2	1518	4376	20.4	3.61	16.64	17.78	19.23	21.59
Tumor 3	484	1586	41.7	2.75	16.64	15.75	18.74	20.23
Tumor 4	534	1270	22.5	2.79	10.44	9.29	13.03	12.13
Tumor 5	1443	3770	6.89	4.80	26.66	27.26	31.96	30.26
Tumor 6	1188	2744	12.9	3.45	18.58	18.57	18.59	18.28
Tumor 7	1417	3674	20.1	2.74	9.95	9.57	10.7	10.25
Tumor 8	1842	4264	14.2	3.14	8.06	8.44	8.94	9.25
Tumor 9	713	1883	29.6	2.64	15.44	15.69	18.43	19.46
Tumor 10	4680	12,531	3.81	4.66	23.58	22.49	28.22	27.86
Tumor 11	5937	14,170	1.65	3.34	8.34	8.29	10.25	8.44
Tumor 12	1125	2650	12.0	2.51	8.19	7.86	8.88	9.31
LN 1	381	914	12.6	3.37	15.8	19.14	20.97	21.43
LN 2	381	681	5.01	2.72	4.42	4.7	4.77	5.29
LN 3	725	1792	19.1	2.25	5.68	5.32	6.1	6.69
LN 4	524	1481	18.3	1.96	5.12	4.56	4.65	4.9
LN 5	879	1561	7.09	2.43	5.1	4.95	6.49	5.34
LN 6	678	1275	6.57	2.58	5.63	6.91	7.24	7.56
LN 7	815	1440	5.31	1.69	2.17	2.98	2.61	3.05
LN 8	946	2287	14.1	6.38	82.67	81.31	100.01	96.44
LN 9	820	2044	19.7	2.43	7.54	6.68	8.34	9.21
Tumor V_{diff}	-	-	-	-	0%	−1.1%	+13.5%	+12.9%
LN V_{diff}	-	-	-	-	0%	+1.8%	20.2%	+ 9.2%

Abbreviations: ITV = internal target volumes; PROPCPS = proportional to counts per second.

Target intensity, diameter, motion, and ITVs (cm^3) of tumors and lymph nodes. Intensity values were averaged across all gating methods; units are PROPCPS. Net target motion was calculated by the difference of target centroids between end-inhale and end-exhale phases using method A1. End-exhale images with method A1 were used to estimate the longest axis of the target as the target diameter. V_{diff} represents the average algorithm volume percentage difference relative to T1.